The Cosmic Origins Spectrograph FUV Detector.

Jason B. McPhate, Oswald H. Siegmund, Geoff Gaines, John V. Vallerga, and Jeff Hull

The University of California, Berkeley, Space Sciences Laboratory,
Berkeley, CA 94720-7450, USA

ABSTRACT

The Far Ultraviolet (FUV) detector for the Cosmic Origins Spectrograph (COS), scheduled to be installed in the Hubble Space Telescope in June 2003, is currently being built by the Experimental Astrophysics Group at The University of California, Berkeley. The COS FUV detector system is based on the detectors flown on the Far Ultraviolet Spectroscopic Explorer (FUSE) satellite with changes to take advantage of technological improvements since the development of those detectors. The COS FUV detector is a dual segmented, cylindrical input face, MCP detector with cross delay line (XDL) readouts. Each segment is a Z-stack of MCPs with an active area 85 mm by 10 mm. The segments are abutted end to end to form a total active area approximately 180 mm by 10 mm (with a gap in the middle). Detector spatial resolution in the long (spectral) dimension is better than 25 microns and in the short dimension (cross-dispersion) is better than 50 microns. The MCPs are coated with a CsI photocathode to achieve the optimal quantum detection efficiency (QDE) in the 1150-1750 angstrom bandpass. Improvements in the understanding of the processing required to produce higher QDE MCPs has lead to significant improvements in the FUV QDE relative to previous missions. This paper presents the basic design parameters and performance characteristics of the COS FUV detector.

Keywords: FUV, Detectors, MCPs, XDL, COS, HST

1. INTRODUCTION

The Cosmic Origins Spectrograph[1] (COS) is a fourth generation instrument for the Hubble Space Telescope (HST) and is scheduled to be installed as an axial bay instrument aboard HST in mid 2003. COS is designed to achieve scientific goals[2] (*e.g.*, origin of large scale structure in the Universe, evolution of galaxies, origins of stellar and planetary systems) that require very high efficiency and moderate spectral resolution ($R \geq 20,000$). COS has two spectroscopic channels, one in the near-ultraviolet (NUV) covering the 1750–3200 Å region and the other in the far-ultraviolet (FUV) covering the 1150–1775 Å bandpass, and uses a modified Rowland circle spectrograph design with holographically ruled, astigmatism corrected, aspherical (to correct for the HST optical system aberrations) gratings. This paper is concerned with the detector system for the FUV channel which is currently being built by the Experimental Astrophysics Group of the University of California, Berkeley Space Sciences Laboratory (UCB-SSL).

The approach of this paper will be to first give a description of the FUV detector system and briefly how it fits into the COS instrument. We will then present measured performance characteristics of an electrical test unit (ETU) that has been used at UCB-SSL for final system optimization.

The FUV detector system for COS was originally specified as a "build to print" of the detector systems[3] currently on orbit in the Far Ultraviolet Spectroscopic Explorer (FUSE), albeit with a CsI photocathode rather than the FUSE KBr photocathode to improve sensitivity in the longer wavelength bandpass of COS. However, since the design and fabrication of the FUSE detectors, several areas of potential performance improvement were found and exploited. These changes primarily concern the position encoding electronics, but also address system sensitivity and throughput. These changes will be discussed in the context of performance enhancements relative to the FUSE detectors.

Further author information: (Send correspondence to J.B.M.)
J.B.M.: E-mail: mcphate@ssl.berkeley.edu
O.H.S.: E-mail: ossy@ssl.berkeley.edu
G.G: E-mail: ggaines@ssl.berkeley.edu
J.V.V.: E-mail: jvv@ssl.berkeley.edu
J.H.: E-mail: jeffh@ssl.berkeley.edu

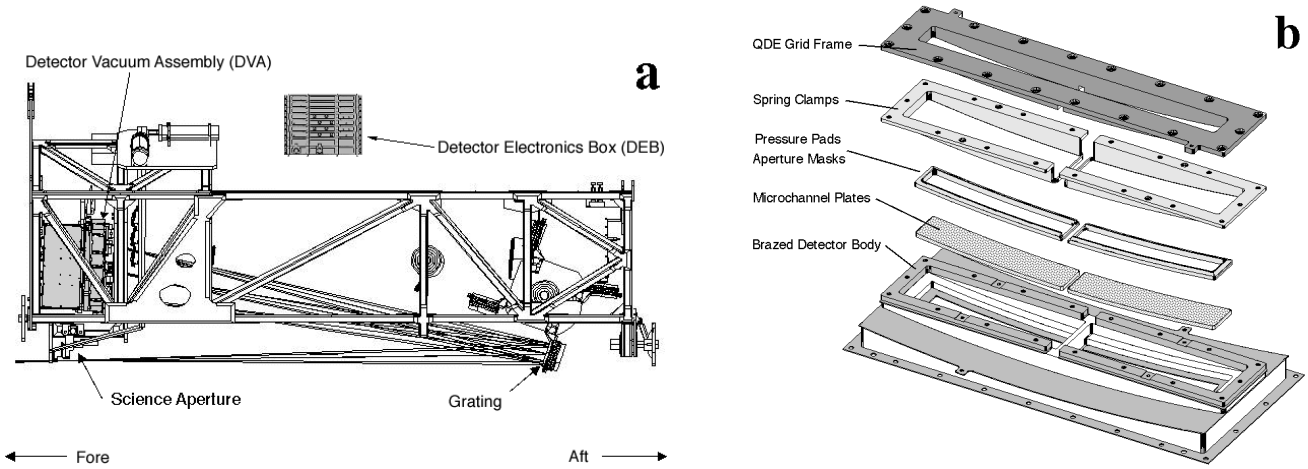

Figure 1. **a** Schematic of the COS instrument showing the locations of the FUV detector subsystem components. **b** Schematic representation of a brazed body assembly (BBA).

2. DESCRIPTION

The COS FUV detector system is a windowless, FUV photon counting device employing an opaque photocathode deposited on microchannel plates (MCPs) to convert photons to electrical pulses. A charge cloud produced by the MCPs is collected by a delay line anode and the resulting signals are amplified and processed by microwave application electronics to produce position information. The detector system is comprised of two main physical components, the detector vacuum assembly (DVA) and the detector electronics box (DEB). The DVA is effectively the detector head, housing the MCPs, anodes, and amplifiers. This is located in the COS instrument cavity such that the spectrally dispersed light from the gratings is focused on the input face of the MCPs (see Fig. 1a). The DEB contains the position encoding electronics, microprocessor, and power supplies and is located about 2 m from the DVA (Fig. 1a).

2.1. Detector Vacuum Assembly

The DVA is built around the detector backplate (effectively the optical bench of the system) and consists of a vacuum housing which contains the detector brazed body assembly, the amplifiers for the signals from the anodes, and a high voltage filter module.

The detector brazed body assembly (BBA) consists of a ceramic and kovar brazed body which houses two end-to-end, MCP segments each with an active area of 85 mm × 10 mm (spectral by spatial), with a 8 mm gap between the active areas (see Figs. 1b and 2a). The input face of the MCPs are curved (826 mm radius) to match the COS Rowland circle, maintaining optical focus over the entire active area of the detector (both segments). Each segment is a Z-stack of 95 mm × 20 mm Photonis low noise, high resistance MCPs with 80:1 l/d, and 19° pore bias angles. Each stack contained a single 12 μm pore diameter (15 μm pitch) and two 10 μm pore (12.5 μm pitch) plates. The stacks are operated at a gain of $\sim 10^7$ electrons per event. The pore sizes were mixed to reduce Moiré fringing effects in flat field images. To further reduce Moiré patterns the hexagonal multi-fiber pattern of the 12 μm plates were "clocked" 30° relative to those of the 10 μm plates.[4] For flight the input surface of the MCPs will be coated with an opaque CsI photocathode and a negatively biased quantum detection efficiency (QDE) enhancement grid will be used to drive photo-electrons produced on the MCP webbing into an adjacent pore.

The electron clouds produced by each MCP intensifier segment are accelerated by a rear field potential onto a helical cross delay line (HXDL) anode (see Fig. 2b). The charge cloud is sampled in the X (spectral/long) dimension by the X helical delay line itself. In Y (spatial/short) dimension the charge cloud is sampled by long conductive strips which are connected to the Y helical outside the active area. The charge fractions for the X and Y delay lines are roughly 70% and 30% , respectively. Each pulse is split into four components, one traveling in each direction down both delay lines. The timing of the output signals from the two ends of a delay line gives the location in that dimension where the initiating charge cloud landed. The single pass delay for these anodes is typically 80 ns and

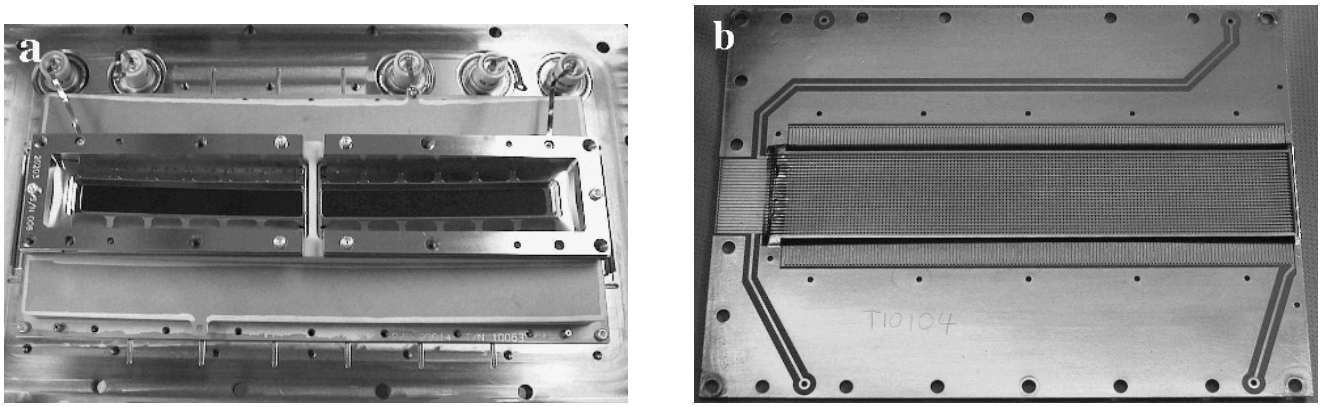

Figure 2. **a** Picture of a flight candidate brazed body assembly without QDE enhancement grid. **b** Picture of a flight candidate HXDL anode.

10 ns in the X and Y dimensions, respectively. Each signal is fed into a low power, fast, two stage amplifier with interstage filtering before being sent to the DEB where the position encoding is done. Each amplifier set (four fast channels) also contains a charge summing channel to produce a pulse for monitoring the total charge in each event.

The high voltage used to bias the MCPs is provided by a high voltage power supply (HVPS) in the DEB, but is not delivered directly to the detector. Instead a high voltage filter module (HVFM) located next to the amplifiers on the detector backplate receives two voltages from the HVPS (one for each segment), and distributes these voltages around the detector (one rear field accelerating voltage, two independent MCP stack voltages, and two independent QDE grid bias voltages) as well as providing further filtering and ripple reduction.

The vacuum housing in which the BBA is enclosed has a deployable vacuum door covering the optical input aperture. This door can be opened and closed with a motor mechanism, and will be opened once during flight. If the door motor mechanism should become jammed there is a high output paraffin (HOP) actuator and spring mechanism for backup door release. Furthermore, this HOP actuator mechanism can be re-armed if the motor becomes unjammed. This scenario is unexpected as many (thousands) of door open-close cycles were performed during door testing for the FUSE project. The door allows the DVA interior to be kept at vacuum when the exterior is at atmosphere while still allowing the detector to be run windowless when the DVA is in a vacuum environment. Two 4 liter per second ion pumps are mounted on the vacuum housing to maintain vacuum inside the DVA during integration and testing, and to generally keep the detector at vacuum from the time the MCPs are conditioned until close to launch. These ion pumps will be flown, but will not be operated on orbit. Two small windows over each segment in the door allow for detector liveliness testing while the DVA is not enclosed in a vacuum environment.

A grid is placed at the entrance aperture of the vacuum housing (vacuum door aperture) and biased to +15 VDC to repel any thermal ions that may be in the spectrograph cavity. A Mu-metal enclosure is placed around the BBA to attenuate magnetic fields in the detector area, thus reducing any image shifts that could be caused by changing magnetic fields.

2.2. Detector Electronics Box

The DEB consists of two time to digital converters (TDCs) for each segment (four total), the detector control electronics (DCE), a low voltage power converter (LVPC), and the HVPS. All power system components (LVPC, HVPS, and HVFM) are provided by Battel Engineering. The LVPC receives bus voltage from the COS instrument and converts this to the proper power levels and provides filtering and regulation. The HVPS produces two independent HV outputs which go to the HVFM.

For a good description of the basic operation and optimization of MCP delay line systems see to Ref. 5. The esential operation is as follows. The timing signals from the amplifiers in the DVA arrive at the TDCs where each is input into a constant fraction discriminator (CFD). Each CFD produces a fast logic transition that is coincident with the incoming pulse. For each dimension, one such pulse starts a time to amplitude converter (TAC), and the other stops it. The pulse that is used to stop the TAC is first put through a lump delay module to guarantee its arrival

at the TAC after the undelayed pulse, independent of the location of the initiating charge cloud on the the delay line. The voltage on the TAC integrator is then sampled by an analog to digital converter (ADC). Both the X and Y dimension use 16-bit ADCs. However, only 14 bits (16,384 values) of X data and 10 bits (1,024 values) of Y data are used for the final position values. A 6 bit dithering scheme is used in X to reduce the effect of non-uniform ADC bin sizes. For each X and Y TDC pair there is a 8 bit total charge digitization circuit. Seven bits of this digitized value is used. After the ADCs have converted the TAC signals the TACs are reset to a reference voltage to prepare for the next event. If another event arrives before the current event is processed the second event is rejected.

The digitized values are then passed along to the DCE, a 8051 processor based flight computer running assembly language code. It is responsible for communications with the COS instrument electronics, interpretation and execution of commands, housekeeping monitoring and packaging (thermistors, voltages, HV, *etc.*), and some science data processing. The DCE receives digitized data from both segments asynchronously. It must merge these two data streams into one data stream and keep track of any losses that occur at high count rates. This last task is accommodated by keeping track of data counters at various locations in the science data stream. Five counters are kept, two fast event counters (FECs), two digital event counters (DECs), and a total event counter (TEC). The FECs (one for each segment) are very low deadtime ($\sim$300 ns per event) counters that keep track of essentially every time the TAC could have been started. The DECs (one for each segment) are the actual number of events that are digitized by the TDC. They represent the number of counts coming into the DCE. The two segment data streams are merged with a round robin scheme. The TEC is the number of events coming out of the round robin and can be less than the sum of the two DECs if the count rate is high enough to overflow the round robin. The system deadtime has been held to a minimum while maintaining a throughput curve that can be easily understood under numerous observing conditions.

3. PERFORMANCE CHARACTERISTICS

Testing has been performed on flight or flight like versions all components of the system. Currently all mechanical and electrical components are meeting or exceeding requirements. At this time flight parts are being integrated into what will be the final flight system. Then final optimization, conditioning, and testing will be performed. We present here the results from tests performed on flight candidate MCPs and an electrical test unit version of the TDCs.

3.1. Microchannel Plate Performance

We received 11 sets of low noise, matched high resistance ($\sim$ 35 MΩ per plate) MCPs from Photonis (a set being one 12 μm pore plate, and two 10 μm pore plates). All sets of MCPs performed well in initial testing, but with some sets being marginally better than others. Preliminary selection of flight MCPs was performed based on pulse height distribution (PHD) uniformity, low background rate, and minimization of "hot spots" and dead spots. These plates perform quite well. They have background rates that are less than 0.5 count cm^{-2} s^{-1} straight out of dry N_2 storage. There are no hot spots, no large dead spots, and a minimal number of small dead spots. The PHDs are very uniform, with full width at half maximums (FWHMs) of less than 50% of the modal gain ($\sim 10^7$ electrons per event) for uniform full field illumination.

We found that the 10 μm plates did not have QDEs high enough to fulfill the sensitivity goals of COS, but the 12 μm plates did. Furthermore, the QDEs of all the 12 μm MCPs were found to be very consistent. An example of the QDE for normally incident extreme ultraviolet (EUV) light of a bare 12 μm MCP is plotted in Fig. 3a. Fig. 3b shows the QDE for normally incident FUV light in the COS bandpass for a 12 μm MCP coated with $\sim$ 16,000 Å of CsI. Based on the exceptional QDEs achieved with the 12 μm plates we chose to build the COS flight stacks with a 12 μm plate on top. A concern with stacking the plates with the 12 μm plate above two 10 μm plates (12-10-10 stack) is that Moiré fringe reduction obtained by using mixed pore size plates and clocking the multi-fiber patterns may be lost. However, recent deep flat fields of a flight candidate BBA with the plates stacked in a 12-10-10 configuration reveal no evidence of Moiré fringing to approximately the 5% level.

3.2. Detector Electronics Performance

The electrical test unit (ETU) version of the TDC electronics is a commercial parts version of the initial layout design. Through the course of testing with this unit several changes were made that affected the circuit layout, primarily that of the TAC. Apart from the use of commercial parts these layout changes are the only differences

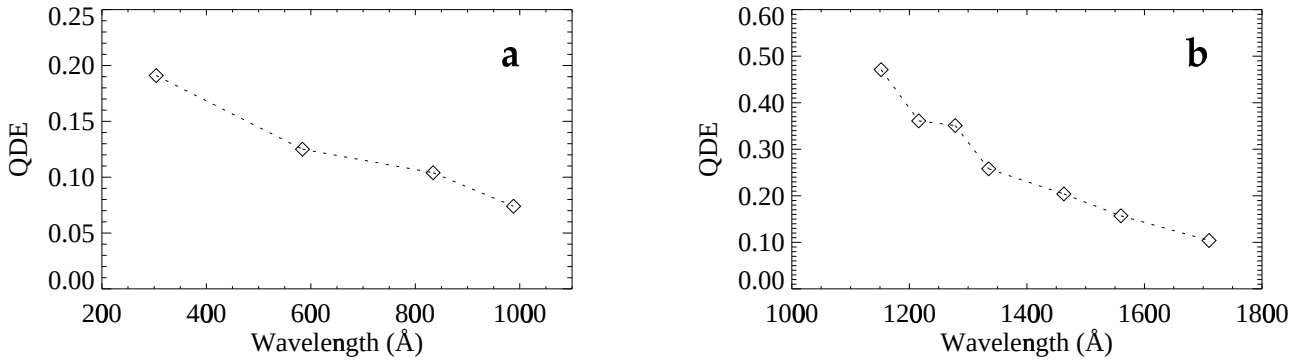

Figure 3. **a** Quantum detection efficiency of a bare 12 μm pore flight candidate MCP to normally incident EUV light. **b** QDE to normally incident FUV light of a 12 μm flight candidate MCP coated with $\sim 16,000$Å of CsI (a QDE enhancement grid was used).

between the ETU and the flight boards. The performance of the ETU should be representative of the performance of the flight TDCs, with the possible exception that the cleaner flight layout might improve performance.

The ETU was used to verify the performance of the the system against several metrics. These included, (1) detector spatial resolution as a function of position on the detector, in both axes, (2) linearity of the position response across the detector in the X direction, (3) measured resolution as a function of input count rate, and (4) count rate throughput for a single segment as a function of input rate. Each of these is discussed in the following sub-sections.

3.2.1. Resolution verses position

The resolution of the detector system to photon stimulus is tested by placing a thin ($\sim$ 10 μm) electro-formed Ni mask in direct contact with the front surface of the input MCP and illuminating the detector with light from a Hg pen-ray lamp. The standard mask that we employ is opaque except of an array of 10 μm diameter pinholes on 500 μm centers. The disadvantage of this mask is that a single pinhole in the mask can illuminate one, two, or even three pores of the MCP. This results in a large scatter in the measured FWHM of the pinholes over the face of the detector. Moreover, the frequency of the pinholes can beat with that of the MCP pores, causing entire regions of the detector to have measured FWHMs that are not truly representative of the detector performance. To reduce the scatter associated with the small pore number sampling of the pinhole masks, we use a mask that has a significantly larger input function, then deconvolve out the known input function from the measured FWHM. We chose a mask with an input function similar to that which will be placed on the detector by the COS optical system. These masks consist of three rows of 25 μm $\times$ 500 μm rectangular "slits" on 200 μm centers in X (the rows are separated by 2.5 mm). This mask was used to determine the detector resolution in the X dimension, the data are plotted in Fig. 4a. The average measured FWHM of 31 μm is equivalent to a deconvolved detector resolution of 25 μm. This value is commensurate with the COS requirement of 25 μm resolution over 80% of the detector in X. To measure the resolution in Y dimension the pinhole mask had to be used, this data is presented in Fig. 4b. The resolution in Y is equivalent to that in X, and far exceeds the required 50 μm specification.

3.2.2. Positional response linearity

An advantage of using the electro-formed masks is that the spacing of the illumination pattern on the detector is very well known and linear. By comparing the spacing of measured centroids to the expected spacing we achieve a measurement of the linearity of the detector system. The difference between the measured and expected separations yields the detectors deviation from linearity. The data for this test performed on the ETU are plotted in Fig. 5. The perturbation at the right side of the plot is caused by signal reflections at the anode-feedthrough interface coming back and disturbing the pulse baseline at the ends of the field of view.[5] Even this bump is within about 20 μm of linearity, well within the $\pm$100 μm over 80% of the detector requirement. The remaining features in this plot may be residual non-linearities of the detector system or mask.

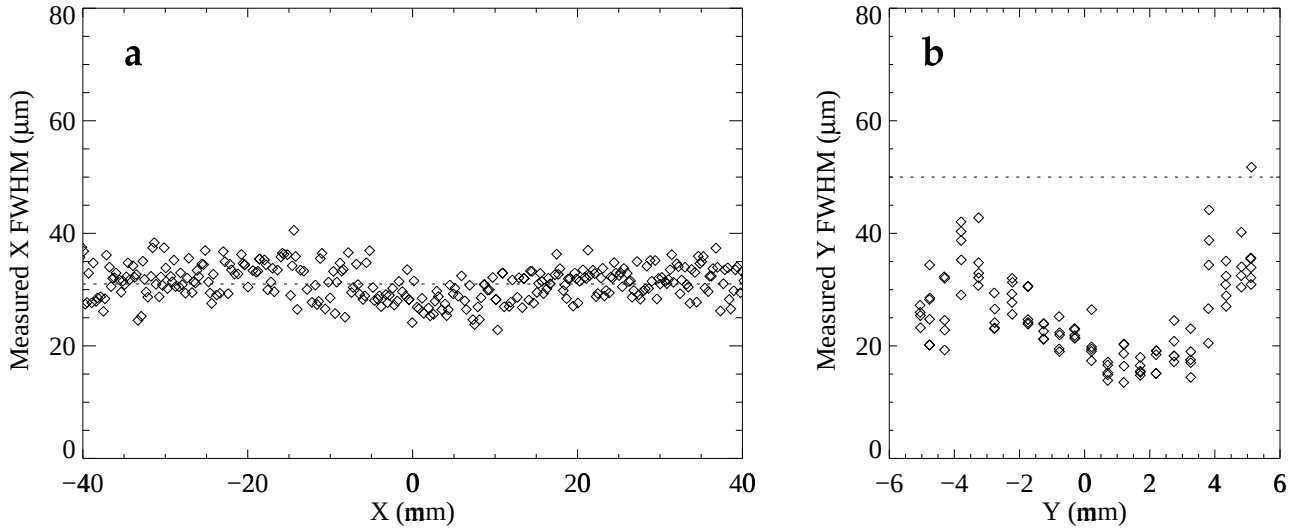

Figure 4. **a** Measured X (spectral) FWHM for 25 μm $\times$ 500 μm input slits as a function of X position on the detector. The average FWHM of 31 μm is equivalent to a detector resolution of 25 μm. **b** Measured Y (spatial) FWHM for 10 μm diameter input pinholes as a function of Y position.

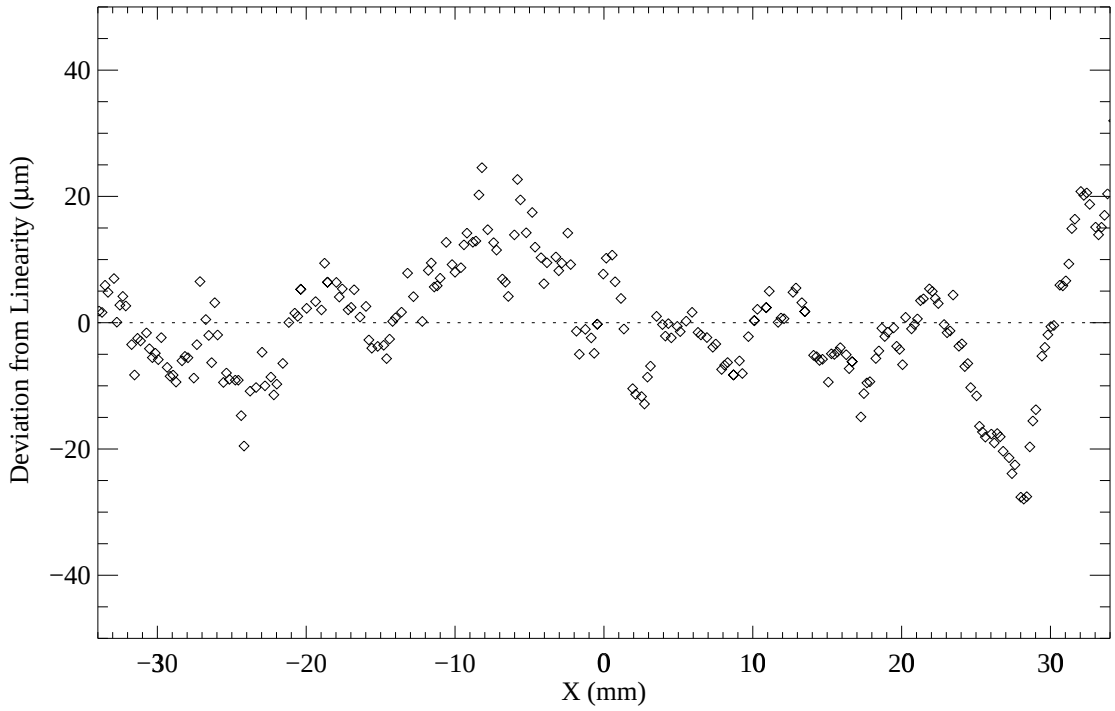

Figure 5. Deviation from linearity in the X position over 80% of the detector active area. These data were derived by taking the differences of the expected slit spacings for the 25 μm slit mask and the measured separations.

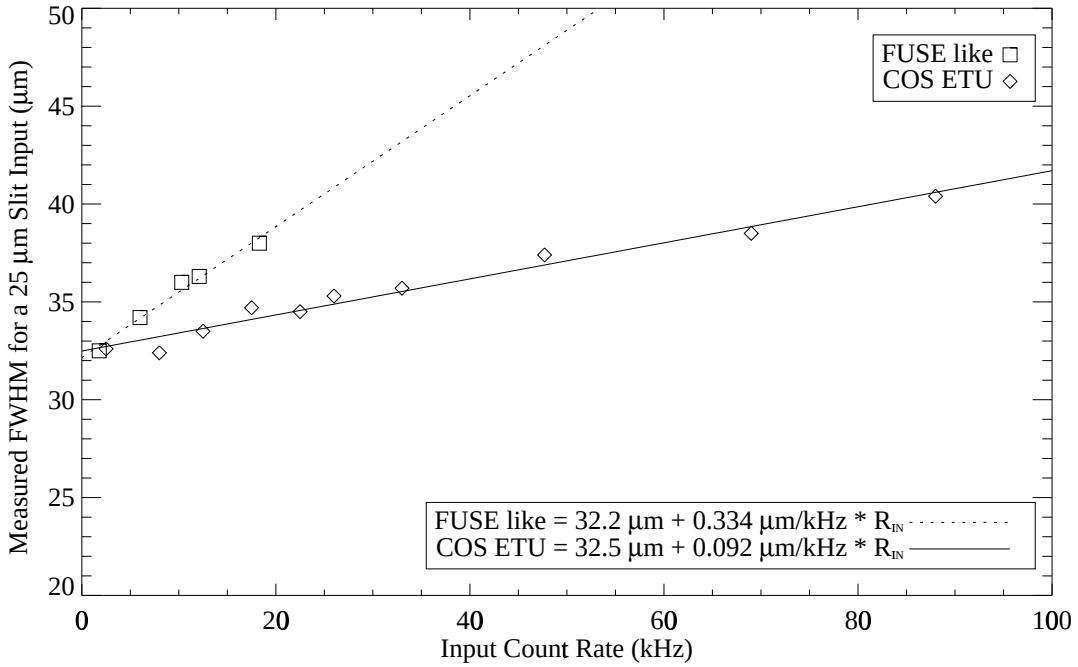

Figure 6. Degradation of the measured FWHM of a 25 μm slit input function as a function of input count rate for the COS ETU and a FUSE like circuit. Linear fits to each data set are over-plotted.

3.2.3. Resolution verses count rate

After the FUSE detectors were built and delivered it was discovered that the detector resolution degraded at high counting rates. This was traced to the TAC circuit, specifically to an interaction between the current TAC event signal and the tail of the reset of the previous event. A modification to the TAC integration starting, stopping, and reseting scheme was made which improved the resolution performance at higher rates. The average measured FWHM for the 25 μm slit mask is plotted as a function of input rate in Fig. 6. The data represented by squares is the results obtained from the FUSE like circuit (*i.e.,* before the TAC modification was made), and the diamonds are the results acquired after the TAC was modified. The lines are linear fits to the data and the associated equations are printed on the graph. The new circuit still degrades with rate, but with a slope less than one-third that of the FUSE like circuit. Although most of the COS science is expected to be performed at low counting rates, it was decided it was worth the effort to change the TDC layout to implement this circuit to maintain a more scientifically flexible instrument. The layout options for the FUSE style TAC circuit were left in place to permit a return to that design should a failure occur with the newer design during subsequent testing.

3.2.4. Detector electronics throughput

The FUSE detectors used double delay line (DDL) anodes for readout which require a charge division to determine the Y location of an event and timing (a TDC) for the X location. The charge to digital converters (CDCs) needed for the Y dimension are inherently slower than the timing channel TDC. This means that the deadtime of the FUSE system is dominated by the CDC operation. Therefore, by going to a HXDL anode COS has replaced the slower Y dimension CDC with a fast TDC and so reduced the electronics deadtime. This results in a significant improvement in electronics throughput at higher input counting rates. The output count rates as a function of input count rates for the FUSE flight spare system and the COS ETU are plotted in Fig. 7. Both curves are for a single segment under uniform full field illumination.

The curves plotted over the data are simple models using two different types of deadtime, paralyzable and non-paralyzable.[6] Non-paralyzable deadtime occurs when an event arrives during the processing of the previous event,

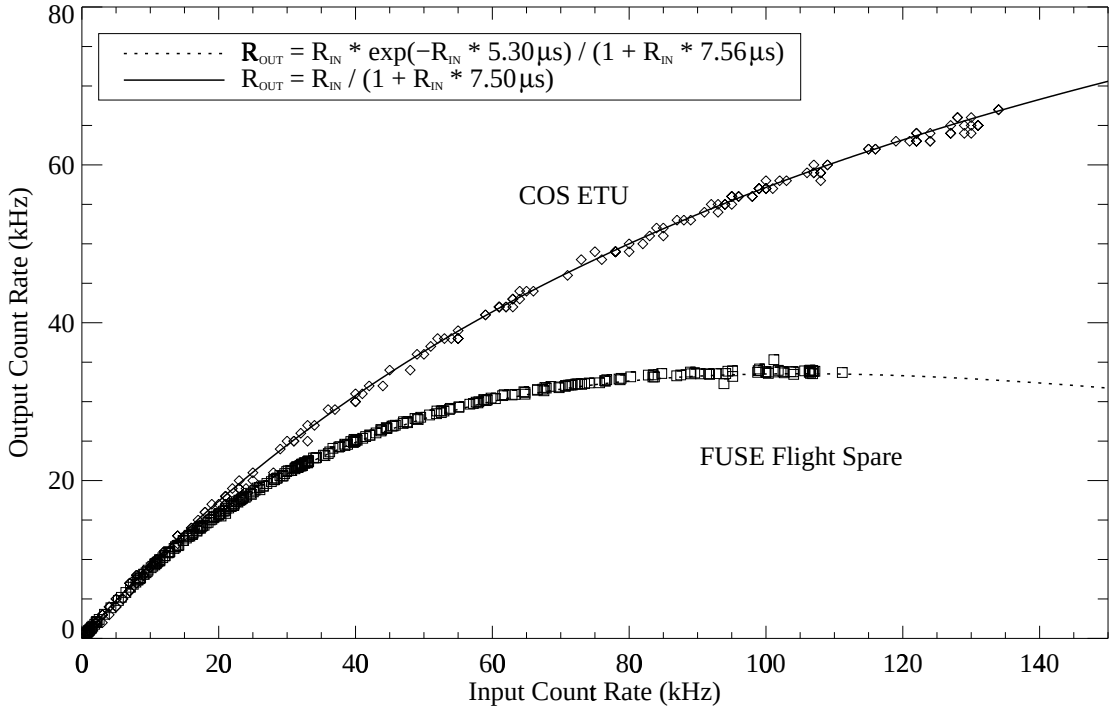

Figure 7. Throughput of the COS ETU system and the FUSE flight spare system with models over-plotted.

and only the second event is lost. Paralyzable deadtime occurs when both events are discarded, because the nature of the system causes corruption of the first event by the second (*e.g.,* "collision" of the slow charge pulses in the FUSE system). Because the FUSE system used a slow (twice times several μs) charge channel it is susceptible to charge pile-up at high rates and therefore must monitor when dual events occur during the charge conversion window and discard both counts. The probability of a second event not occurring during this window is just the Poisson probability for zero events in that time for input rate, $R_{\rm IN}$. That is

$$P_{\rm P} = exp(-R_{\rm IN} \cdot \tau_{\rm P}). \tag{1}$$

This is the probability of throughput for the paralyzable portion of the FUSE event processing. Because COS does not use a charge channel for position determination there is no equivalent paralyzable deadtime in the system from event collision. Even if two events occur within the roughly 80 ns propagation delay of the anode a single miss-imaged event will occur (with the start from one signal and the stop from the other). The deadtime for a non-paralyzable system (like COS, and the remaining portion of the FUSE system) is just $R_{\rm OUT} \cdot \tau_{\rm N}$, so the probability of outputting a count is

$$P_{\rm N} = 1 - R_{\rm OUT} \cdot \tau_{\rm N} = \frac{1}{1 + R_{\rm IN} \cdot \tau_{\rm N}}. \tag{2}$$

For a system with both paralyzable and non-paralyzable parts, like the FUSE system, the total probability of producing a count is just the product of the two components. Using these equations to match the throughput data for the FUSE and COS systems produces deadtimes that are very close to those expected from analysis of the timing of the state machine logic that controls the event propagation through the digitizer electronics. See Fig. 7 for the values of these parameters for both systems.

4. CONCLUDING REMARKS

While the COS FUV detector system was initially proposed as a "build to print" copy of the FUSE detector systems it has undergone enough modification to be considered its own design. A host of small modifications were made to improve the performance relative to the FUSE detectors where possible and to tailor the performance for the

different requirements of the COS instrument. The microchannel plates chosen for this detector are performing well. An electrical test unit of the detector electronics has been used to prove the performance of the design in the areas of resolution, position linearity, and throughput. All flight parts will be in house within the next month and system integration has begun. We are on schedule to deliver the flight detector system to Ball-Aerospace in January 2001.

ACKNOWLEDGMENTS

This research was funded by NASA HST-COS grant NAS 5-98043 through a subcontract with the University of Colorado at Boulder Center for Astrophysics and Space Astronomy.

REFERENCES

1. J. A. Morse, J. C. Green, D. C. Ebbets, J. P. Andrews, S. R. Heap, C. Leitherer, J. L. Linsky, B. D. Savage, J. M. Shull, T. P. Snow, S. A. Stern, J. T. Stocke, and E. Wilkinson, "Performance overview and science goals of the Cosmic Origins Spectrograph for the Hubble Space Telescope," Proc. SPIE **3356**, pp. 361–368, Aug. 1998.
2. J. C. Green and J. A. Morse, "Progress report on the Cosmic Origins Spectrograph," in *American Astronomical Society Meeting*, vol. 195, pp. 9207+, Dec. 1999.
3. O. H. Siegmund, M. A. Gummin, J. M. Stock, G. Naletto, G. A. Gaines, R. Raffanti, J. Hull, R. Abiad, T. Rodriguez-Bell, T. Magoncelli, P. N. Jelinsky, W. Donakowski, and K. E. Kromer, "Performance of the double delay line microchannel plate detectors for the Far-Ultraviolet Spectroscopic Explorer," Proc. SPIE **3114**, pp. 283–294, Oct. 1997.
4. A. S. Tremsin, O. H. W. Siegmund, M. A. Gummin, P. N. Jelinsky, and J. M. Stock, "Electronic and optical moiré interference with microchannel plates: artifacts and benefits," Appl. Opt. **38**, pp. 2240–2248, Apr. 1999.
5. J. V. Vallerga and J. B. McPhate, "Optimization of the readout electronics for microchannel plate delay line anodes," Proc. SPIE **4139**, *This Volume.*
6. M. Lampton and J. Bixler, "Counting efficiency of systems having both paralyzable and nonparalyzable elements," *Rev. Sci. Instruments* **56**, pp. 164–165, Jan. 1985.